



**Reconstruction of crystal band structure by spectral caustics in high-order harmonic generation**Jiaxiang Chen <sup>1</sup>, Qinzhi Xia,<sup>2,\*</sup> and Libin Fu <sup>1,†</sup><sup>1</sup>Graduate School of China Academy of Engineering Physics, No. 10 Xibeiwang East Road, Haidian District, Beijing 100193, China<sup>2</sup>Institute of Applied Physics and Computational Mathematics, Beijing 100088, China

(Received 11 May 2021; accepted 26 November 2021; published 10 December 2021)

We propose a method to retrieve the band structure by measuring the caustic points of the harmonic spectrum generated by the interaction between laser and solid. The relation between the energy  $\omega_c$  of the spectral caustic points and the external fields  $F$  encodes the bandgap of the solid. Specifically, for a simple band structure,  $\varepsilon_g(k) = \varepsilon_0 + \varepsilon_1[1 - \cos(ka_0)]$ , according to the semiclassical theory, we map the crystal momentum  $k_c$  to the caustic point energy  $\omega_c$  by  $F$  since  $k_c$  is independent of the parameters  $\varepsilon_0$  and  $\varepsilon_1$ . Furthermore, for the general band structure, because its first-order form is a simple energy band, we can roughly retrieve the first-order form of the energy band and obtain the accurate band structure by iterative calculation. Using this method, we solve the deviation between the retrieved and the target bandgap near the Brillouin zone boundary. Also, we show that this method is suitable for wide-bandgap materials.

DOI: [10.1103/PhysRevA.104.063109](https://doi.org/10.1103/PhysRevA.104.063109)**I. INTRODUCTION**

The band structure is an essential property of the material responsible for explaining the electrical properties of a material. At present, the primary method of measuring the energy band structure in experiments is angle-resolved photoemission spectroscopy (ARPES) [1]. Recently, the high-order harmonic spectrum generated by the interaction between a laser and a solid is expected to be a supplement to ARPES and become a new all-optical nondestructive detection method for the energy band mechanism of materials [2–5].

The spectral structure of high-order harmonic generation (HHG) in solids is shown to be sensitive to the crystal band structure, including multiple plateaus [6–8], cutoff frequency [9–12], and anisotropy [13–15]. Based on these properties, the HHG spectrum can be used to reconstruct the band structure of the material. Recently, Li *et al.* [5] presented a temporal Young's interferometer and demonstrated its application in retrieving the band structure of ZnO in which the interference fringes of the harmonic spectrum can be predicted by semiclassical theory. The three-step model of solids successfully explains the generation of interband harmonics, where the semiclassical motion of an electron-hole pair is determined by the band structure and external field [16,17] and provides a new method for band reconstruction [5].

However, many issues and challenges have arisen during the process of band reconstruction based on semiclassical theory. For example, a wide bandgap gives rise to a large frequency shift of the harmonic spectrum, while for a narrow bandgap, the frequency shift can be neglected. Particularly, for insulators, a small increase in the bandgap will cause a significant frequency shift of the HHG spectrum peak, which

will affect the position of the interference fringes in the HHG spectrum. In addition, the retrieved bandgap shows a significant deviation from the target near the boundary of the Brillouin zone (BZ). In this paper, to reduce the deviation of the band reconstruction at the Brillouin zone boundary and overcome the influence of the wide bandgap, we propose a new reconstruction method using spectral caustics of HHG.

Spectral caustics can be analyzed within the framework of catastrophe theory [18,19]. In the solid HHG spectrum, there are two kinds of caustic enhancement. The first is the van Hove singularity of the energy band structure, where the relative velocity of the electron-hole pair at recombination is 0 [20]. These caustic points are determined by the band structure and can be classified as 'fold' catastrophes. The second kind of caustic enhancement is the coalescence of two or more semiclassical trajectories with the same recombined energy  $\omega$ , where the derivative of  $\omega$  with respect to the birth time of the electron-hole pair,  $t'_s$ , is 0, namely,  $d\omega/dt'_s = 0$  [21]. Compared with the caustics caused by the van Hove singularity, the second kind of caustic point is more easily controlled by the external field. In addition, a stronger enhancement effect can be obtained by coalescing more than two semiclassical trajectories with the help of multicolor external fields [22,23]. Therefore, we choose the second kind of caustics to retrieve the crystal band structure.

In the present work, we investigate spectral caustics with a swallowtail structure in the HHG induced by a nonresonant phase-locked two-color laser pulse. Based on the spectral caustics, we propose a method to retrieve the band structure. The method is shown to be effective for retrieving the band structure by considering ZnO as a sample. For wide-bandgap materials, the retrieving band structure can also reproduce the target bandgap well. A more accurate band structure can be obtained using the general band structure and considering the varying transition dipole moment, the Berry curvature, and the frequency shift. This paper is organized as follows. In

\*xia\_qinzhi@iapcm.ac.cn

†lbfu@gscaep.ac.cn

Sec. II, the theoretical model and reconstruction methods are presented. The results and a discussion are reported in Sec. III, and a brief conclusion is presented in Sec. IV.

## II. THEORETICAL MODEL AND METHODS

We consider a semiconductor that interacts with a laser pulse. The interaction can be described by two-band semiconductor Bloch equations (SBEs) in the length gauge [16,24]. Under the assumption of the Keldysh approximation, the yield of the interband HHG in solid can be expressed as [16,25]

$$J_{\text{er}}(\omega) = \omega \int_{\text{BZ}} dk d(k) \int_{-\infty}^{\infty} dt e^{i\omega t} \int_{-\infty}^t dt' d^*(\kappa_{t'}) F(t') \times e^{-iS(k,t',t)-(t-t')/T_2} + \text{c.c.}, \quad (1)$$

where  $\kappa_{t'} = k - A(t) + A(t')$ ,  $k$  is the crystal momentum, and  $A(t) = -\int_{-\infty}^t F(\tau) d\tau$  is the vector potential with  $F$  as the electric field of the laser pulse.  $d(k) = -i\langle u_c(k) | p | u_v(k) \rangle / \varepsilon_g(k)$  is the transition moment, with  $|u_n(k)\rangle$  representing the periodic part of Bloch states and  $\varepsilon_g(k)$  being the bandgap between the conduction and the valence band at the crystal momentum of  $k$ .  $S(k, t', t) = \int_{t'}^t \varepsilon_g(\kappa_\tau) d\tau$  and  $T_2$  represents the dephasing time.

Compared with the rapid oscillation of  $\exp(-iS + i\omega t)$ , the terms other than the exponent can be regarded as a slowly varying item,  $g(k, t', t)$ . Accordingly, Eq. (1) can be solved using the saddle point approximation and written as

$$J_{\text{er}}(\omega) \propto \sum_{k_s} \frac{g(k_s, t'_s, t_s) e^{-iS(k_s, t'_s, t_s) + i\omega t - (t_s - t'_s)/T_2}}{\sqrt{|S''(k_s, t'_s, t_s)|}}. \quad (2)$$

The points  $(k_s, t'_s, t_s)$  are given by the saddle point equations

$$\frac{\partial S}{\partial k} = \int_{t'}^t \frac{\partial \varepsilon_g(\kappa_\tau)}{\partial k} d\tau = 0, \quad (3a)$$

$$\frac{\partial S}{\partial t'} = -\varepsilon_g(\kappa_{t'}) = 0, \quad (3b)$$

$$\frac{\partial S}{\partial t} = \varepsilon_g(k) + F(t) \int_{t'}^t \frac{\partial \varepsilon_g(\kappa_\tau)}{\partial k} d\tau = \omega, \quad (3c)$$

which describe the classical trajectory of electrons. The determinant of the Hessian matrix is  $|S''| = -a(\kappa_{t'})a(k_s) d\omega/dt'_s$  with  $a(\kappa_\tau) = \partial \varepsilon_g(\kappa_\tau) / \partial k_s$  [21]. Here  $a(\kappa_{t'})$  and  $a(k_s)$  represent the relative velocity of the electron-hole pair at birth and recombination, respectively.  $d\omega/dt'_s$  is the derivative of the recombined energy with respect to the birth time of the electron-hole pair.

For direct-bandgap materials, the electron-hole pair is born approximately at the minimum bandgap corresponding to  $a(\kappa_{t'}) = 0$ . At the same time, the electric field is generally nonzero at  $t'_s$ , namely,  $F(t'_s) \neq 0$ . Therefore, a singularity also appears when the trajectories satisfy the condition [21]

$$\frac{d\omega}{dt'_s} = \frac{\partial \varepsilon_g(k_s)}{\partial k_s} + F(t_s) \int_{t'_s}^{t_s} \frac{\partial^2 \varepsilon_g(\kappa_\tau)}{\partial k_s^2} d\tau = 0. \quad (4)$$

As can be seen,  $d\omega/dt'_s$  depends on the energy band structure and the external field. Thus we can modulate the caustic points by adjusting the external field,  $F$ . In addition, we denote the saddle point that satisfies Eq. (4) as  $(k_c, t'_c, t_c)$ .

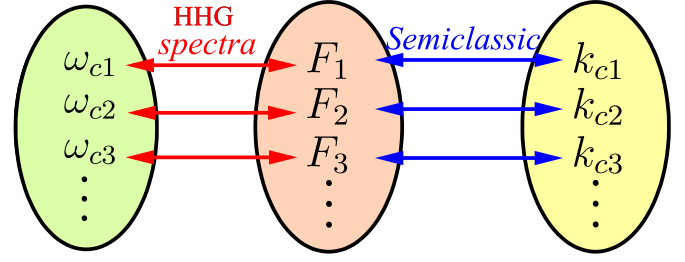


FIG. 1. The red (left) [blue (right)] arrows denote the mapping relation between the electric field  $F$  and the harmonic energy  $\omega_c$  (crystal momentum  $k_c$ ) at the caustic point.

Here we consider two cases. The first one is for a simple band structure, namely,  $\varepsilon_g(k) = \varepsilon_0 + \varepsilon_1[1 - \cos(ka_0)]$ . In this case, we find that the caustic point is independent of  $\varepsilon_0$  and  $\varepsilon_1$  through analysis of Eqs. (3a), (3b), and (4), which means that the mapping relation of  $F$  and  $k_c$  can be obtained with the help of the semiclassical theory (see blue arrow in Fig. 1). At the same time, the caustic point energy  $\omega_c$  can be read from the harmonic spectrum (see red arrow in Fig. 1). By choosing the appropriate external field, we can ensure that there is only one caustic point on the harmonic spectrum for each field strength. As a result, the dependence of  $\varepsilon_g$  on  $k_c$  can be obtained according to Eq. (3c).

The other case is for the general band structure. We expand the bandgap with Fourier series,

$$\varepsilon_g(k) = \varepsilon_0 + \sum_{i=1}^N \varepsilon_i [1 - \cos(ika_0)], \quad (5)$$

and set  $N$  to 3, while higher-order terms can also be studied in the same way. Since the caustic points of the semiclassical prediction and the experimental measurement have a certain derivation, we choose the iterative method to solve Eqs. (3a)–(3c) and Eq. (4) instead of solving them directly with four caustic points.

First, set the dispersion relation as  $\varepsilon_g^T(k) = \varepsilon_0 + \varepsilon_1[1 - \cos(ka_0)]$ , which contains the first-order term of the Fourier expansion of the general band structure. Second, substitute  $\varepsilon_g^T(k)$  into Eqs. (3a)–(3c) and Eq. (4) and obtain the crystal momentum-dependent harmonics,  $\omega_c(k_c)$ . Third, fit  $\omega_c(k_c)$  with  $\varepsilon_g(k)$  [Eq. (5)]. Finally, set  $\varepsilon_g^T(k) = \varepsilon_g(k)$  and repeat the second and the third steps until reaching the convergent dispersion relation [see Eq. (5)], namely, a set of solutions of  $\varepsilon_i$  is convergent.

During the reconstruction of the ZnO and square lattice band structure (see in Sec. III), we find that the convergence rate is rapid if the term  $i = 1$  dominates the high-order terms, i.e.,  $\varepsilon_1 > \varepsilon_2, \varepsilon_3, \dots, \varepsilon_N$ . The reason is that we use  $\varepsilon_g^T(k) = \varepsilon_0 + \varepsilon_1[1 - \cos(ka_0)]$  as the initial approximation of our iteration. Domination of  $\varepsilon_g(k)$  by the higher-order term may cause the convergence rate to slow down. In this case, our simple iteration can be improved by applying some other optimization methods such as the quasi-Newton method or conjugate gradient method. In the following, we show an example to verify this reconstruction method.

We choose three-dimensional (3D) ZnO as the target material interacting with collinearly polarized two-color laser

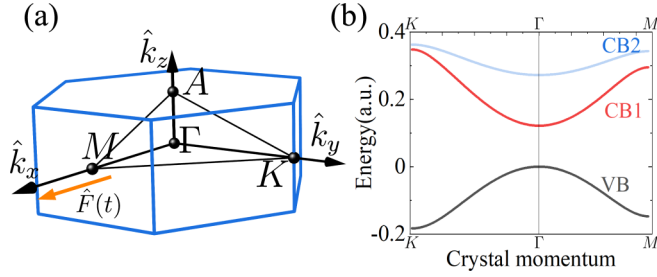


FIG. 2. (a) First Brillouin zone of ZnO (wurtzite structure). (b) Band structure of ZnO along  $\Gamma$ - $M$  and  $\Gamma$ - $K$ .

pulses, consisting of the fundamental wave (FW) and its second harmonic (SH). Figure 2(a) shows the orientation of the reciprocal lattice for ZnO (wurtzite structure) where  $\hat{x} \parallel \Gamma$ - $M$ ,  $\hat{y} \parallel \Gamma$ - $K$ ,  $\hat{z} \parallel \Gamma$ - $A$  (optical axis). The lattice constant  $(a_x, a_y, a_z) = (5.32, 6.14, 9.83)$  a.u., the reciprocal lattice vector  $(b_x, b_y, b_z) = (\pi/\sqrt{3}a_x, 4\pi/3\sqrt{3}a_x, 2\pi/a_z)$ , and other band structure parameters can be found in Ref. [26]. Although the interband HHG is mainly generated by the transition between the highest valence band and the first conduction band (CB1), three bands are considered in the simulation.

The multiband SBEs in the length gauge can be expressed as [21,24]

$$i\partial_t \rho_{nm'}^{\hat{k}}(t) = - \left( \varepsilon_n^{\hat{k}}(t) - \varepsilon_{n'}^{\hat{k}}(t) + i \frac{(1 - \delta_{nn'})}{T_2} \right) \rho_{nm'}^{\hat{k}}(t) + \hat{F}(t) \cdot \sum_m [\hat{d}_{mn}^{\hat{k}}(t) \rho_{mm'}^{\hat{k}}(t) - \hat{d}_{n'm}^{\hat{k}}(t) \rho_{nm}^{\hat{k}}(t)], \quad (6)$$

where  $\rho_{nm'}^{\hat{k}}$  is the density matrix element with initial crystal momentum  $\hat{k}$ ,  $\varepsilon_n^{\hat{k}}(t)$  is the energy of the  $n$ th band at  $\hat{k} + \hat{A}(t)$ , and  $n = v, c_i$  for the highest valence band and the  $i$  conduction band, respectively. The  $\hat{k}$ -dependent dipole  $\hat{d}_{nm}^{\hat{k}}$  is calculated by  $d_{nm}^{\hat{k},j}(t) = \sqrt{E_{p,j}/2} [\varepsilon_{nm}^{\hat{k}}(t)]^2$ , where  $j = x, y, z$  and  $E_{p,j}$  are the Kane parameters. Here, we set the dephasing time  $T_2 = T_0/2$  and  $T_0$  is the period of the FW. The electric field of the collinearly polarized two-color pulses in which the polarization of the FW and the SH are along the  $\hat{x}$  axis [orange arrow line in Fig. 2(a)] can be written as

$$\hat{F}(t) = F_0 [\cos(\omega_0 t) + R \cos(2\omega_0 t + \varphi)] f(t) \hat{x}, \quad (7)$$

where  $R$  is the ratio of the amplitude of the SH to the FW fields and  $\varphi$  is the phase delay. The carrier frequency of the FW is  $\omega_0 = 0.0117$  a.u. and the envelope  $f(t)$  is trapezoidal, with five cycles at peak intensity (3-5-3). The high harmonic spectrum is obtained from the Fourier transform of the time-dependent induced current  $\hat{J}(t)$ ,

$$I(\omega, F_0) \propto |\mathfrak{F}\{t[\hat{J}(t) \cdot \hat{n}]\}|^2, \quad (8)$$

where  $\hat{n}$  is the unit vector in the polarization direction.

In this work, we hope to retrieve the bandgap between CB1 and the valence band for ZnO. Besides, since the polarization direction of the external field is along the symmetry axis  $\hat{x}$  and the bandgap of ZnO is structurally symmetrical, the classical action of electron-hole pairs can be regarded as 1D.

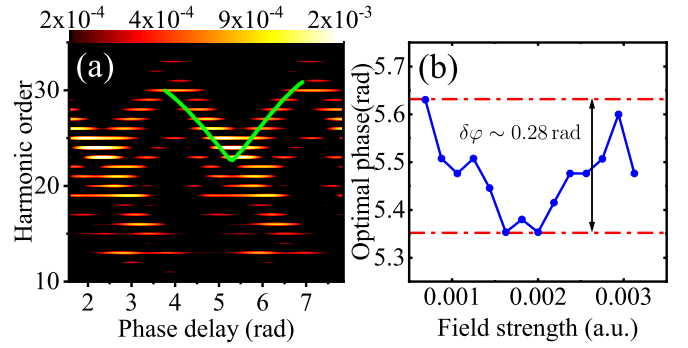


FIG. 3. (a) HHG spectra as a function of the phase delay  $\varphi$  for  $R = 0.48$  and the field amplitude  $F_0 = 0.002$  a.u. The green line represents the caustic line predicted by the semiclassical theory. (b) Optimal phase of the caustic enhancement as a function of the field strength for  $R = 0.48$ .

### III. RESULTS AND DISCUSSION

In this section, first, we present the optimal phase for different field strengths. Second, we show the results of retrieving the bandgap of ZnO using the methods proposed in Sec. II and prove that this method is robust to the focal volume averaging (FVA) of HHG. Third, we verify that this method is suitable for wide-bandgap materials. Finally, we show that the reconstruction method works for a band structure with degeneracy or a cross.

#### A. The optimal phase

Figure 3(a) shows the HHG spectra obtained by numerically solving SBEs as a function of the phase delay  $\varphi$  for  $F_0 = 0.002$  a.u. and  $R = 0.48$ . The color scale ranges from the brightest to one-tenth of the brightest. As the phase delay increases, the harmonic order at the caustic points presents a swallowtail structure (the caustic line). This caustic line can be well predicted by the semiclassical theory [see green line in Fig. 3(a)]. We focus on the most caustic enhancement (brightest point in the diffraction pattern), located near the convergence of the caustic line. Figure 3(b) shows the optimal phase corresponding to the brightest point of the HHG spectra in Fig. 3(a) for different field strengths. For the field parameters used here, the optimal phase is in the range of 5.36 to 5.64 rad as the field strength increases.

Generally, the dispersion relation near the high symmetric point, such as  $\Gamma$ , can be approximated as a quadratic function of the crystal momentum, so the position of the singularity is determined by the three parameters  $(R, \varphi, \omega)$  which are independent of the field strength. In other words, the optimal phase is fixed. The small oscillation of the optimal phase (0.28 rad) in Fig. 3(b) results from the nonquadratic dispersion relation far away from the high symmetric point. Here we should point out that the HHG spectrum has caustics for any phase delay and can be used for band reconstruction. The reason for the choice of  $R = 0.48$  and  $\varphi = 5.5$  rad in the following calculations is that the caustic point near the optimal phase has a better enhancement conducive to experimental measurements.

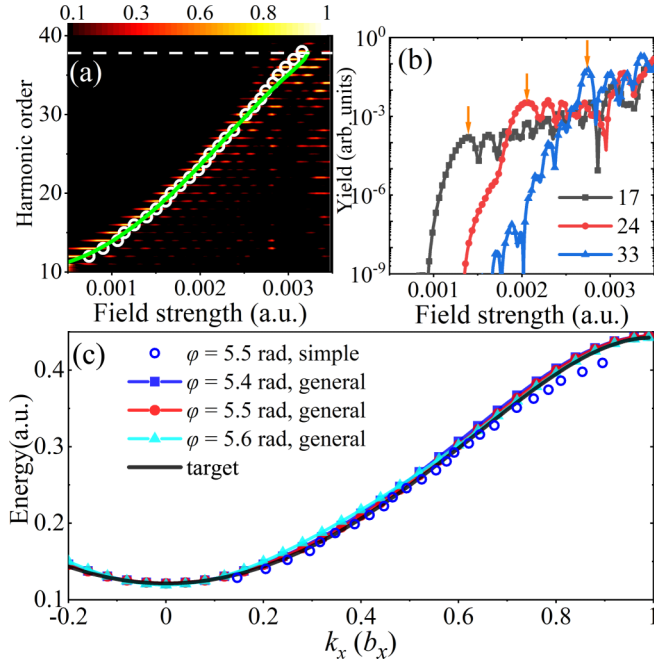


FIG. 4. (a) Normalized HHG spectra as a function of the field strength  $F_0$  for  $R = 0.48$  and the phase delay  $\varphi = 5.5$  rad. The horizontal dashed white line is the maximum bandgap between the valence and the conduction band, and the open white circles mark the maximum HHG yield for each field strength. The solid green line represents the caustic line predicted by semiclassical theory. (b) The intensity of HHG as a function of the field strength for the 17th (black squares), 24th (red circles), and 33rd (blue triangles) harmonics. (c) Target (solid black line) and retrieved momentum-dependent bandgap. Open blue circles represent the retrieved bandgap for a simple band structure. Filled blue squares, red circles, and cyan triangles represent the retrieved bandgaps with Eq. (5) for phase delay  $\varphi = 5.4, 5.5,$  and  $5.6$  rad, respectively.

### B. Bandgap reconstruction of ZnO

Figure 4(a) shows the normalized HHG spectrum as a function of the FW field strength. The spectrum has been divided by the maximum HHG intensity between 10th and 45th order at each field strength value. The caustic points [see the open white circles in Fig. 4(a)] read from the HHG spectra and the caustic line [see solid green line in Fig. 4(a)] predicted by the semiclassical theory are in remarkable agreement. Both of them show that the caustic point energy in the HHG spectrum can cover the entire bandgap with adjustment of the FW strength, while the caustic enhancement disappears when the harmonic energy is greater than the maximum bandgap [see dashed white line in Fig. 4(a)]. This suggests that we can directly read the maximum bandgap from the HHG spectra.

As shown in Fig. 4(a), the caustic points depend on both the field strength and the harmonic order. However, the harmonic order at the caustic point is discrete [see Figs. 3(a) and 4(a)]. Therefore, for convenience, we read the caustic point from the HHG yield as a function of the field strength for a fixed harmonic order. Figure 4(b) shows the HHG yield with respect to the field strength for the 17th, 24th, and 33rd harmonics. As can be seen, as  $F_0$  increases, the plateau appears. We regard the

field strength at the first peak on the plateau as the position of the caustic point [see orange arrows in Fig. 4(b)].

Figure 4(c) shows the band structure using the reconstruction method presented above. For comparison, the target bandgap is also plotted [see the solid black line in Fig. 4(c)]. In the case of a simple band, the retrieved band structure [see the open blue circles in Fig. 4(c)] well reproduces the target bandgap when the crystal momentum is close to  $\Gamma$  ( $k_x = 0$ ), namely,  $k_x < 0.7 b_x$ , while it deviates from the target bandgap when  $k_x > 0.7 b_x$ . The deviation is proportionate to  $k_x$  and it is caused by omission of the higher-order terms of the dispersion relation. To get a more accurate reconstructed band, we also consider the higher-order terms of the dispersion relation [see Eq. (5)]. In the iterative calculation process, we fixed the maximum value of the bandgap, which can be read from Fig. 4(a) with an error of less than one photon energy. The resulting bandgaps for different phase delays (filled blue squares, red circles, and cyan triangles) are in remarkable agreement and all of them show that an accurate bandgap can be reconstructed using the reconstruction method. A more accurate bandgap can be obtained by considering the higher-order terms.

### C. Focal-volume averaging

In the above simulation, only a single field strength is considered. However, since the intensity distribution of the focused laser beam is spatial non-uniform, the actual experimental result includes the emitted harmonics induced by lasers of various intensities. To further illustrate the feasibility of this method in the experiment, focal volume averaging (FVA) has to be taken into account in the simulations. Therefore, the total harmonic spectrum at a peak field strength  $F_0$  is written as

$$\bar{I}(\omega, F_0) = \int_0^{F_0} I(\omega, F) \frac{\partial V}{\partial F} dF. \quad (9)$$

For simplicity we choose the form  $\partial V/\partial F$  as [27]

$$\frac{\partial V}{\partial F} \propto \frac{1}{F} \left( \frac{F_0^2}{F^2} + 2 \right) \sqrt{\frac{F_0^2}{F^2} - 1}. \quad (10)$$

Though the form can be improved by considering the shape and volume of the solids or the interference effect, we can see that our method is robust to the average because of the very sharp caustic transition.

Specifically, Fig. 5(a) shows the field strength dependence of the 17th-, 24th-, and 33rd-order harmonic after considering the FVA with filled black squares, red circles, and blue triangles, respectively. For comparison, the field strength dependence of the 17th-order harmonic corresponding to the single field strength is shown again with the dotted-dashed black line. The orange arrow denotes the caustic field strength  $F_c$  of  $17\omega_0$ . As can be seen, the interference oscillation has been smoothed by the average. However, the transition from the very low yield of HHG with  $F < F_c$  to the plateau yield with  $F > F_c$  corresponds to the transition from the “dark side” of the caustic to the “bright side” [28,29]. The very sharp caustic transition makes it easy for us to determine  $F_c$  through the inflection point of  $\bar{I}(\omega, F_0)$ . Using the caustic point reading from the HHG spectra, including the FVA effect, we achieve



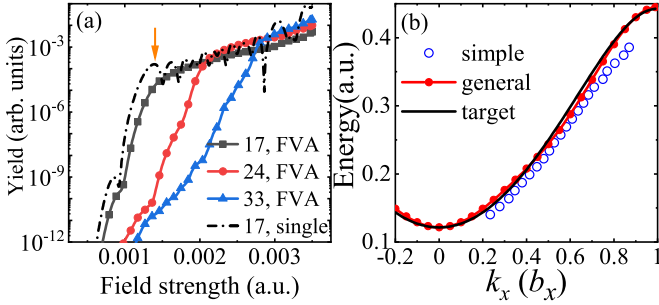


FIG. 5. (a) The intensity of HHG as a function of the field strength for the 17th-order (black squares), 24th-order (red circles), and 33rd-order (blue triangles) harmonics after considering the focal volume average, respectively. The dotted-dashed line is the same as the black squares in Fig. 4(b). (b) Target bandgap (solid black line) and retrieved momentum-dependent bandgaps using a simple (open blue circles) and a general (filled red circles) band structure.

a good reconstruction of the bandgap [see solid black line and open blue circles in Fig. 5(b)].

#### D. Wide-bandgap material

The method is also applicable to reconstruction of a large bandgap. Figure 6(a) shows the HHG spectra for a large bandgap, where we manually increase the width of the bandgap to  $\varepsilon_g(k) \rightarrow \varepsilon_g(k) + 5\omega_0$ . Compared to the case of a narrow bandgap [see open white circles in Fig. 4(a)], the caustic points for the wide bandgap [see open white circles in Fig. 6(a)] are shifted upward by about  $5.5\omega_0$ . The extra shifted frequency  $0.5\omega_0$  is caused by the widening of the bandgap. The caustic enhancement disappears at the 44th-order harmonic, which covers the entire bandgap in this case, allowing us to reconstruct the band structure. As shown in Fig. 6(b), the result of the simple band assumption still reconstructs the target bandgap of the wide bandgap well for  $k_x < 0.7b_x$ . In the case of the general band, the retrieved bandgap is in good agreement with the target bandgap near the Brillouin zone boundary and  $\Gamma$ . The maximum deviation between the retrieved and the target bandgaps is only about 0.01 a.u. ( $\approx 0.03b_x$ ) at  $k_x \approx 0.4b_x$ .

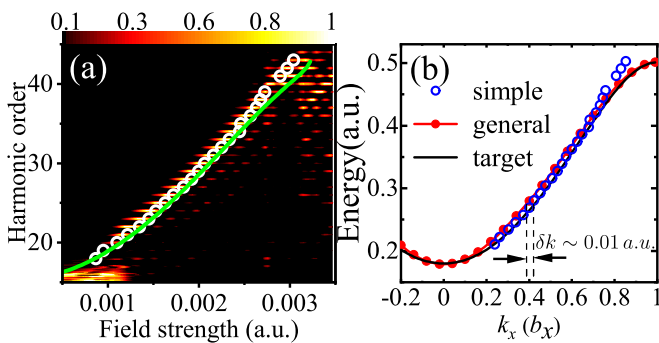


FIG. 6. (a) Normalized HHG spectra as a function of the field strength for the bandgap as  $\varepsilon_g(k) \rightarrow \varepsilon_g(k) + 5\omega_0$ . The field parameters used are the same as in Fig. 4(a). (b) Target (solid black line) and retrieved momentum-dependent bandgaps using a simple (open blue circles) and a general (filled red circles) band structure.

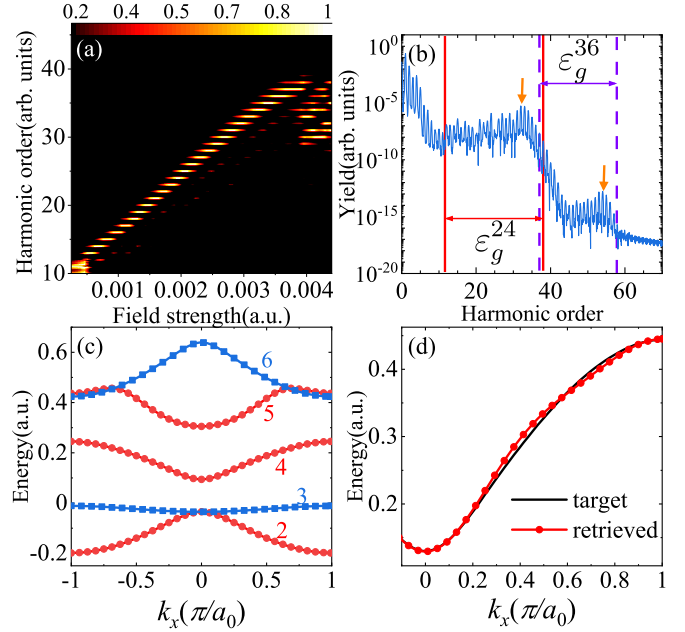


FIG. 7. (a) Normalized HHG spectra as a function of the field strength  $F_0$  for  $R = 0.48$  and phase delay  $\varphi = 5.5$  rad. (b) HHG spectrum of the  $F_0 = 0.003$  a.u. section. The left (right) solid red line is the minimum (maximum) bandgap between the second and the fourth bands. The left (right) dashed purple line is the minimum (maximum) bandgap between the third and the sixth bands. (c) The second to sixth bands of a two-dimensional square lattice. (d) Retrieved bandgap (filled red circles) and target bandgap (solid black line).

The reconstruction method in this paper does not account for the frequency shift. The frequency shift can be estimated by assuming that the frequency shift of each harmonic order is the same. As a result, the caustic structure read from the HHG spectra remains unchanged and the band structure can be approximated as  $\varepsilon_g(k_s) = \varepsilon_0^t + \varepsilon_1^t [1 - \cos(k_s a)]$ . Additionally, according to Eq. (4),  $k_s$  is independent of the simple band structure, so that the band structure can be solved by choosing two caustic points. Accordingly, the overall frequency shift caused by the bandgap can be estimated as  $\Delta\varepsilon_0 = \varepsilon_0^t - \varepsilon_0^l$ , where the exact minimum bandgap  $\varepsilon_0^l$  can be accurately measured with linear optical methods.

#### E. Two-dimensional square lattice

In this subsection, we further show the effect of multi-bands on the reconstruction method with spectral caustics. Figure 7(c) shows the second to sixth bands of the 2D square lattice along  $\Gamma$ -X, where the periodic potential of the 2D square lattice  $V(x, y) = -0.4(1 - \cos \frac{2\pi x}{a_0})(1 - \cos \frac{2\pi y}{a_0})$  and  $a_0 = 6$  a.u. Initially all electrons are in valence bands, namely, the second and third bands. According to the solution of the Schrödinger equation, only bands with the same color have dipole-allowed couplings. The ratio  $R$  and the phase delay  $\varphi$  of the electric field are 0.48 and 5.5 rad, respectively.

Figure 7(a) shows the normalized HHG spectra for the 2D square lattice. The caustic energy range of the HHG above

the minimum bandgap is  $12\omega_0$  to  $38\omega_0$ , corresponding to the minimum ( $\varepsilon_{g,\min}^{24} \approx 11\omega_0$ ) and maximum ( $\varepsilon_{g,\max}^{24} \approx 38\omega_0$ ) bandgap between the second and the fourth bands, respectively. Therefore, the caustics of HHG spectra in Fig. 7(a) are generated by the transition between the second and the fourth bands.

The multiband effect is demonstrated in the HHG spectrum in Fig. 7(b). Two plateaus appear in the spectrum. The HHG intensity at the cutoff frequency ( $\omega_{\text{cut}}$ ) [see orange arrows in Fig. 7(b)] shows a significant enhancement. The HHG intensity difference between the two plateaus is about six orders of magnitude because  $\varepsilon_{g,\min}^{36}$  (or  $\varepsilon_{g,\min}^{25}$ ) is much greater than  $\varepsilon_{g,\min}^{24}$ . Therefore, we can distinguish multiple caustic points caused by multiple bands and reconstruct the bandgap  $\varepsilon_g^{24}(k)$ .

We can see that, though the energies of the states at the cross are the same, the symmetries [see filled red circles and blue squares in Fig. 7(c)], velocities, and effective masses of the states are different. Therefore, HHG caustics originating from the coupling between the second and the fourth bands can be distinguished. The result of the retrieved bandgap using the caustics at the first plateau is shown in Fig. 7(d) by the filled red circles. The good agreement between the retrieved and the target bandgap shows that the method works for the band structure with degeneracy.

In addition, we should point out that the transition between the third and the fourth bands in the 2D square lattice is only strictly forbidden on the symmetry axis, and the other points are dipole-allowed. In the solution of the SBEs, two factors suppress HHG related to these regions and make the approximation used here reasonable. First, we denote the crystal momentum of the electron-hole pair at birth as  $(k_{xb}, k_{yb})$ , then an increase in  $|k_{yb}|$  will cause an increase in  $\varepsilon_g^{34}(k_{xb}, k_{yb})$ , which leads to a rapid decay of the electron tunneling rate. Second, the electrons and holes there have opposite nonzero transverse velocities preventing them from recollision and harmonics generation.

#### IV. CONCLUSION

In summary, we have proposed and verified a method to reconstruct the band structure of material using the caustic points of the HHG spectra. This method is based on a multitrajectory coalescence in which electron-hole pairs are born and recombined at zero separation and have the same recombined energy. Here, we show that the retrieved bandgaps are in remarkable agreement with the target bandgaps for wurtzite ZnO and a 2D square lattice.

For more general materials, many bands are degenerated or crossed, which puts some limitations on our approach. It has been noted that besides different symmetries, these crossed

bands usually have different effective masses. The different effective masses lead to different tunneling and diffusion rates [30,31], which strongly influence the HHG progress. When the symmetries and effective masses cannot distinguish the multiple crossed bands, our method cannot reconstruct the band structure because more than two bands are entangled and contribute significantly to the same plateau. When the symmetries and effective masses can help us distinguish the two dominated bands from the many crossed bands, our method is applicable to material with spatial inversion symmetry, and it is robust to the FVA of the field strength, such as the ZnO and 2D square lattice discussed in this work. Besides, although the cutoff frequency of each HHG plateau has caustic enhancement and could be used for multiband reconstruction, HHG on the second or higher plateau may come from multiple paths, such as sequential and direct excitation, which prevents direct application of the present method.

Three additional factors should be mentioned: the varying transition dipole moment, the Berry curvature, and the frequency shift. The simulations in this work include the varying transition dipole moment and the frequency shift. These two factors do not affect the band reconstruction in this work, illustrated by the good agreement between the retrieved and the target bandgaps in ZnO and a 2D square lattice, which is consistent with Ref. [21]. For wide-band materials, the additional caustics arising from the rapidly varying dipole moment may become important and cannot be neglected, so we should consider the varying transition dipole moment in the semiclassical analysis following the approach outlined in Ref. [31]. Also, the model considered in this work has spatial inversion symmetry, and thus the Berry curvature vanishes. Materials without spatial inversion symmetry will exhibit an interband transition dipole phase as well as an intraband Berry phase [31–35], resulting in additional terms in the classical action. In this case, the semiclassical analysis of electron-hole pairs, including the abnormal velocity arising from the Berry phase, can follow the approach proposed in Ref. [36]. In future work, we will consider these three factors further to improve the reconstruction method and make it feasible for more general materials.

#### ACKNOWLEDGMENTS

J. Chen thanks L. Xu and L. Jia for helpful suggestions. The authors also acknowledge valuable support from the National Natural Science Foundation of China (Grants No. 11725417, No. 11974057, No. 12088101, and No. U1930403), and Science Challenge Project (Grant No. 2018005).

- 
- [1] A. Damascelli, Z. Hussain, and Z.-X. Shen, Angle-resolved photoemission studies of the cuprate superconductors, *Rev. Mod. Phys.* **75**, 473 (2003).  
 [2] G. Vampa, T. J. Hammond, N. Thiré, B. E. Schmidt, F. Légaré, C. R. McDonald, T. Brabec, D. D. Klug, and P. B. Corkum, All-

Optical Reconstruction of Crystal Band Structure, *Phys. Rev. Lett.* **115**, 193603 (2015).

- [3] T. T. Luu, M. Garg, S. Y. Kruchinin, A. Moulet, M. T. Hassan, and E. Goulielmakis, Extreme ultraviolet high-harmonic spectroscopy of solids, *Nature (London)* **521**, 498 (2015).

- [4] A. A. Lanin, E. A. Stepanov, A. B. Fedotov, and A. M. Zheltikov, Mapping the electron band structure by intraband high-harmonic generation in solids, *Optica* **4**, 516 (2017).
- [5] L. Li, P. Lan, L. He, W. Cao, Q. Zhang, and P. Lu, Determination of Electron Band Structure Using Temporal Interferometry, *Phys. Rev. Lett.* **124**, 157403 (2020).
- [6] S. Ghimire, A. D. DiChiara, E. Sistrunk, P. Agostini, L. F. DiMauro, and D. A. Reis, Observation of high-order harmonic generation in a bulk crystal, *Nat. Phys.* **7**, 138 (2011).
- [7] G. Ndashimiye, S. Ghimire, M. Wu, D. A. Browne, K. J. Schafer, M. B. Gaarde, and D. A. Reis, Solid-state harmonics beyond the atomic limit, *Nature (London)* **534**, 520 (2016).
- [8] C. Yu, H. Irvani, and L. B. Madsen, Crystal-momentum-resolved contributions to multiple plateaus of high-order harmonic generation from band-gap materials, *Phys. Rev. A* **102**, 033105 (2020).
- [9] T. Ikemachi, Y. Shinohara, T. Sato, J. Yumoto, M. Kuwata-Gonokami, and K. L. Ishikawa, Trajectory analysis of high-order-harmonic generation from periodic crystals, *Phys. Rev. A* **95**, 043416 (2017).
- [10] L. A. Chizhova, F. Libisch, and J. Burgdörfer, High-harmonic generation in graphene: Interband response and the harmonic cutoff, *Phys. Rev. B* **95**, 085436 (2017).
- [11] N. Tancogne-Dejean, O. D. Mücke, F. X. Kärtner, and A. Rubio, Impact of the Electronic Band Structure in High-Harmonic Generation Spectra of Solids, *Phys. Rev. Lett.* **118**, 087403 (2017).
- [12] Z. Wang, H. Park, Y. H. Lai, J. Xu, C. I. Blaga, F. Yang, P. Agostini, and L. F. DiMauro, The roles of photo-carrier doping and driving wavelength in high harmonic generation from a semiconductor, *Nat. Commun.* **8**, 1686 (2017).
- [13] Y. S. You, D. A. Reis, and S. Ghimire, Anisotropic high-harmonic generation in bulk crystals, *Nat. Phys.* **13**, 345 (2017).
- [14] K. Kaneshima, Y. Shinohara, K. Takeuchi, N. Ishii, K. Imasaka, T. Kaji, S. Ashihara, K. L. Ishikawa, and J. Itatani, Polarization-Resolved Study of High Harmonics from Bulk Semiconductors, *Phys. Rev. Lett.* **120**, 243903 (2018).
- [15] N. Yoshikawa, K. Nagai, K. Uchida, Y. Takaguchi, S. Sasaki, Y. Miyata, and K. Tanaka, Interband resonant high-harmonic generation by valley polarized electron-hole pairs, *Nat. Commun.* **10**, 3709 (2019).
- [16] G. Vampa, C. R. McDonald, G. Orlando, D. D. Klug, P. B. Corkum, and T. Brabec, Theoretical Analysis of High-Harmonic Generation in Solids, *Phys. Rev. Lett.* **113**, 073901 (2014).
- [17] G. Vampa, C. R. McDonald, G. Orlando, P. B. Corkum, and T. Brabec, Semiclassical analysis of high harmonic generation in bulk crystals, *Phys. Rev. B* **91**, 064302 (2015).
- [18] J. Connor, Catastrophes and molecular collisions, *Mol. Phys.* **31**, 33 (1976).
- [19] Y. A. Kravtsov and Y. I. Orlov, Caustics, catastrophes, and wave fields, *Sov. Phys. Uspekhi* **26**, 1038 (1983).
- [20] A. J. Uzan, G. Orenstein, Á. Jiménez-Galán, C. McDonald, R. E. F. Silva, B. D. Bruner, N. D. Klimkin, V. Blanchet, T. Arusi-Parpar, M. Krüger, A. N. Rubtsov, O. Smirnova, M. Ivanov, B. Yan, T. Brabec, and N. Dudovich, Attosecond spectral singularities in solid-state high-harmonic generation, *Nat. Photon.* **14**, 183 (2020).
- [21] J. Chen, Q. Xia, and L. Fu, Spectral caustics of high-order harmonics in one-dimensional periodic crystals, *Opt. Lett.* **46**, 2248 (2021).
- [22] O. Raz, O. Pedatzur, B. D. Bruner, and N. Dudovich, Spectral caustics in attosecond science, *Nat. Photon.* **6**, 170 (2012).
- [23] D. Faccialà, S. Pabst, B. D. Bruner, A. G. Ciriolo, S. De Silvestri, M. Devetta, M. Negro, H. Soifer, S. Stagira, N. Dudovich, and C. Vozzi, Probe of Multielectron Dynamics in Xenon by Caustics in High-Order Harmonic Generation, *Phys. Rev. Lett.* **117**, 093902 (2016).
- [24] I. Floss, C. Lemell, G. Wachter, V. Smejkal, S. A. Sato, X.-M. Tong, K. Yabana, and J. Burgdörfer, Ab initio multiscale simulation of high-order harmonic generation in solids, *Phys. Rev. A* **97**, 011401(R) (2018).
- [25] L. V. Keldysh, Behavior of non-metallic crystals in strong electric fields, *Sov. Phys. -JETP* **6**, 763 (1958).
- [26] X. Zhang, J. Li, Z. Zhou, S. Yue, H. Du, L. Fu, and H.-G. Luo, Ellipticity dependence transition induced by dynamical Bloch oscillations, *Phys. Rev. B* **99**, 014304 (2019).
- [27] T. Morishita, Z. Chen, S. Watanabe, and C. D. Lin, Two-dimensional electron momentum spectra of argon ionized by short intense lasers: Comparison of theory with experiment, *Phys. Rev. A* **75**, 023407 (2007).
- [28] M. Berry, Waves and Thom's theorem, *Adv. Phys.* **25**, 1 (1976).
- [29] M. Berry, Focusing and twinkling: Critical exponents from catastrophes in non-Gaussian random short waves, *J. Phys. A Gen. Phys.* **10**, 2061 (1977).
- [30] G. Vampa and T. Brabec, Merge of high harmonic generation from gases and solids and its implications for attosecond science, *J. Phys. B At. Mol. Opt. Phys.* **50**, 083001 (2017).
- [31] A. M. Parks, G. Ernotte, A. Thorpe, C. R. McDonald, P. B. Corkum, M. Taucer, and T. Brabec, Wannier quasi-classical approach to high harmonic generation in semiconductors, *Optica* **7**, 1764 (2020).
- [32] D. Xiao, M.-C. Chang, and Q. Niu, Berry phase effects on electronic properties, *Rev. Mod. Phys.* **82**, 1959 (2010).
- [33] H. Liu, Y. Li, Y. S. You, S. Ghimire, T. F. Heinz, and D. A. Reis, High-harmonic generation from an atomically thin semiconductor, *Nat. Phys.* **13**, 262 (2017).
- [34] T. T. Luu and H. J. Wörner, Measurement of the Berry curvature of solids using high-harmonic spectroscopy, *Nat. Commun.* **9**, 916 (2018).
- [35] L. Yue and M. B. Gaarde, Structure gauges and laser gauges for the semiconductor Bloch equations in high-order harmonic generation in solids, *Phys. Rev. A* **101**, 053411 (2020).
- [36] L. Yue and M. B. Gaarde, Imperfect Recollisions in High-Harmonic Generation in Solids, *Phys. Rev. Lett.* **124**, 153204 (2020).